J. Fluid Mech. (2005), *vol.* 545, *pp.* 373–395.
doi:10.1017/S0022112005006890 Printed in the United Kingdom

Theory of two-layer hydraulic exchange flows with rotation

By ULRIKE RIEMENSCHNEIDER[1]†, DAVID A. SMEED[2] AND PETER D. KILLWORTH[2]

[1]School of Ocean and Earth Science, National Oceanography Centre, European Way, Southampton SO14 3ZH, UK

[2]James Rennell Division, National Oceanography Centre, European Way, Southampton SO14 3ZH, UK

(Received 30 September 2004 and in revised form 10 June 2005)

Two-layer rotating exchange flows through channels of rectangular cross-section are modelled using semi-geostrophic, zero-potential-vorticity theory. For a given channel cross-section the full range of possible flow states is considered. The interface always has a uniform slope across the channel, but may separate from one or both of the sidewalls to attach to the upper or lower boundary. The flow may be subcritical, critical or supercritical. These different states are identified in a pseudo-Froude-number plane analogous to that developed by Armi (1986) for non-rotating flows. If the ratio of the channel width to the Rossby radius is constant along the length of the channel, then the solution may be traced along the entire channel using a single diagram. Several examples of maximal and submaximal exchanges are considered. This graphical method of solution is contrasted with the functional approach of Dalziel (1988, 1990).

The exchange flux is determined as a function of the channel geometry, the strength of rotation and the difference in Bernoulli potential between the two layers.

1. Introduction

Exchange flows and the resulting overflows continue to be a widely studied aspect of oceanography. They occur at bottlenecks in the ocean where large oceanic basins are connected only by a small channel through which water masses can be exchanged. Examples include the Strait of Gibraltar, connecting the Mediterranean Sea to the North Atlantic, and the Denmark Strait and the Faroe Bank Channel, connecting the Greenland–Iceland–Norwegian Seas to the North Atlantic. These channels play a crucial role in determining the distribution of water masses around the globe.

Hydraulic theory is the framework which has over the years been consistently used to describe the fundamental characteristics of exchange flows and a variety of versions of this theory with different grades of complexity have been developed. Two-layer exchange flows, without rotation, were discussed by Wood (1970). Later a series of papers by Armi and Farmer (Armi 1986; Armi & Farmer 1986; Farmer & Armi 1986) described non-rotating two-layer exchange in detail for a variety of channel types. These papers explored the flow solutions in the space defined by two Froude

† Present address: Woods Hole Oceanographic Institution, Physical Oceanography Department MS21, Woods Hole, MA 02543, USA.

numbers (one for each layer). Using this approach it was possible, for a given channel geometry and net transport, to illustrate how the flow evolved along the length of the channel on a single Froude-number diagram.

In addition to the graphical representation of the solutions a 'functional approach' was developed by Gill (1977) for a single-layer flow, and later applied to two-layer exchange flows by Dalziel (1990) and Dalziel (1991). The advantage of this method is that it is more easily extended to more complex problems, for example allowing for a non-rectangular cross-section (Dalziel 1992), or a third layer (Smeed 2000). However, other complexities such as continuous stratification, for example, cannot be addressed using this approach (cf. Killworth 1992*b*). Also, by formulating the problem in terms of a functional of a single along-channel variable, the full range of possible solutions was less transparent than in the work of Armi and Farmer.

Dalziel (1990) also considered the effects of rotation and, as we shall also do, he assumed the flow to be semi-geostrophic, with zero potential vorticity, and the channel to be of uniform width connecting wide basins of uniform depth. (These geometrical assumptions are standard in the literature as they grossly simplify the algebra.) In this case he assumed that the secondary control is always located at the exit of the channel.

Both approaches, the functional and graphical, will be used here, and both rely on the same fundamental principles to find *control sections* which essentially determine the flow state at all other sections along the channel. For a full review of the details of the two approaches, we refer the reader to Armi (1986) for the Froude-number planes and Pratt & Helfrich (2005) for the functional approach.

In this paper we examine the problem of zero-potential-vorticity two-layer rotating exchange from a new perspective. We consider solutions as a function of two flow variables, and present the full range of possible solutions in a pseudo-Froude-number plane analogous to that developed by Armi (1986) for non-rotating flows. We also allow the depth and width of the channel to vary together.

The paper is constructed as follows. In § 2 the shallow-water theory describing the two-layer exchange is laid out including all possible situations of interface outcropping. In § 3 the solutions for a narrow and a wider channel are presented using a pseudo-Froude-number plane and maximal as well as submaximal examples are discussed. Also, a more comprehensive overview of controlled fluxes is given for a range of channel widths and Bernoulli potentials. Finally § 4 discusses the limitations and implications of the results.

2. Semi-geostrophic two-layer shallow-water theory with outcropping

Consider a channel of rectangular cross-section, aligned in the x-direction, rotating at a constant angular speed $f/2$, and occupied by two layers of shallow, inviscid, homogeneous fluid of different density. As shown in figure 1, y denotes the across-channel direction and z the vertical direction, while the subscripts $i = 1$ and 2 denote the bottom and top layer respectively. The depth of the channel is $D(x)$, which only varies in the along-channel direction; at its shallowest point its value is D_0. Its width is denoted by $W(x)$, the layer thickness by h_i, and the density by ρ_i, where $\rho_1 > \rho_2$. The interface separating the two layers may ground at some point across the channel or outcrop at the surface, allowing either layer to vanish in some regions of the channel. The pressure in the top layer is denoted by P, and u_i and v_i are the flow velocities in the x- and y-direction respectively.

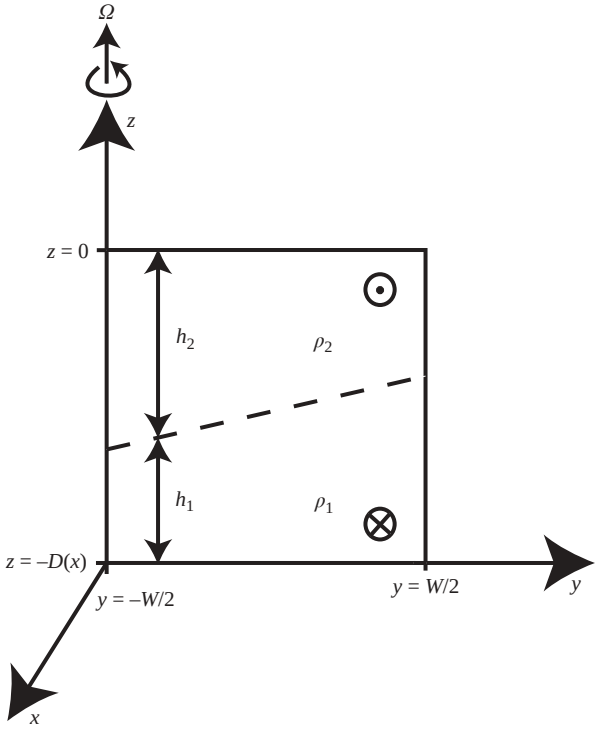

FIGURE 1. Sketch of the cross-section through a rectangular channel with two layers. The thickness of the bottom and top layer is denoted by h_1 and h_2 respectively. Their densities are ρ_1 and ρ_2 with $\rho_1 > \rho_2$. The total depth of the channel is $D(x)$ and its width $W(x)$, both width and depth being dependent only on x. The dashed line indicates the interface separating the two layers, which is linear in the case of zero potential vorticity. The net flow in the bottom layer is in the negative x-direction and that in the top layer in the positive x-direction. The dense reservoir lies at the positive end of the x-axis while the lighter reservoir lies at the negative end.

The shallow-water equations are assumed steady, and will be non-dimensionalized using the Rossby radius, or radius of deformation, defined here as $a_0 = \sqrt{g'D_0}/f$, where g' is the reduced gravity. This yields the following scales:

$$\left.\begin{aligned} (D, h_i, P/g') &= (D, h_i, P)^* D_0, \\ x &= x^* R, \\ (W, y) &= (W, y)^* a_0, \\ u_i &= u_i^* \sqrt{g'D_0}, \\ v_i &= v_i^* \sqrt{g'D_0}\left(\frac{a_0}{R}\right), \end{aligned}\right\} \tag{2.1}$$

where R is a typical along-channel distance and the asterisk marks the non-dimensional variables. Henceforth all equations will be expressed non-dimensionally unless stated otherwise and we will drop the asterisk.

More generally the vertical scale of the flow could be non-dimensionalized using the channel depth at any section along the channel. This would lead to a local Rossby radius $a = \sqrt{g'D}/f$ which will vary along the channel, as the local depth, D, changes.

The parameter

$$L = W\frac{a_0}{a} \tag{2.2}$$

describes the ratio of the channel width to the local Rossby radius. It is also useful to define the variables

$$\hat{u}_i = u_i\frac{a_0}{a} \tag{2.3}$$

which we will refer to as pseudo-Froude-numbers.

We assume the traditional hydraulic semi-geostrophic approximation that the along-channel length scale is significantly larger than the across channel length scale, i.e. the horizontal aspect ratio $\epsilon = a_0/R \ll 1$, which implies that the flow is nearly parallel ($v \ll u$) and that downstream variations are weak ($\partial/\partial x \ll \partial/\partial y$). Then the along-channel momentum equations are geostrophic:

$$u_1 = -\frac{\partial P}{\partial y} - \frac{\partial h_1}{\partial y}, \tag{2.4}$$

$$u_2 = -\frac{\partial P}{\partial y}, \tag{2.5}$$

and it follows that

$$u_2 - u_1 = \frac{\partial h_1}{\partial y}. \tag{2.6}$$

The potential vorticity of the flow is conserved in the two layers, and we assume it is zero:

$$\frac{1 + \partial v_i/\partial x - \partial u_i/\partial y}{h_i} = 0. \tag{2.7}$$

This assumption is equivalent to assuming that the flow originates from infinitely deep reservoirs†. Noting also that the v-component of the velocity vector is very small, due to the traditional sill approximation, the assumption of zero potential vorticity immediately implies that the velocity fields are linear:

$$u_1 = u_{10} + y, \tag{2.8}$$

$$u_2 = u_{20} + y, \tag{2.9}$$

and hence, from (2.6), h_1 is also linear across the channel:

$$h_1 = (u_{20} - u_{10})y + h_{10}. \tag{2.10}$$

Here u_{10}, u_{20} and h_{10} depend only on distance along the channel, and represent the velocities and layer thickness at the centre of the channel, $y = 0$. Equation (2.10) defines the slope of the interface as $h_s = u_{20} - u_{10}$. These zero-potential-vorticity solutions formed the basis for previous studies by Whitehead, Leetmaa & Knox (1974) and Dalziel (1988).

The rigid lid trivially requires

$$h_1 + h_2 = D. \tag{2.11}$$

† Limitations of this assumption will become clear as we develop the theory, but note that Dalziel's (1988) results differed only slightly between zero and constant potential vorticity. We therefore give up the small improvement of the constant-potential-vorticity theory in favour of the mathematically more tractable problem of zero potential vorticity and investigate it in more depth than Dalziel (1988).

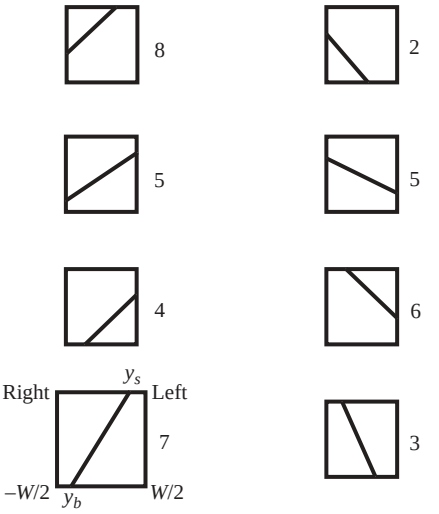

FIGURE 2. Sketches of all possible flow regimes. Regime 5 is *fully attached*, regimes, 2, 4, 6 and 8 are *semi-separated* and regimes 3 and 7 are *fully separated*. In the presentation of the results only regimes with a positive slope (4, 5, 7 and 8) are considered. 'Left-hand' wall refers to the left-hand side of the channel when looking from the lighter towards the denser reservoir in the direction of the net flow of the top layer. The numbering scheme is explained in detail in the Appendix.

In both layers the transport along the channel can now be computed by integrating across the channel; the resulting expressions will depend on the three constants of integration u_{10}, u_{20} and h_{10}, as well as D and W describing the channel geometry:

$$Q_i = \int_{W(x)/2}^{-W(x)/2} u_i h_i \, \mathrm{d}y. \tag{2.12}$$

To reduce the dependence to two constants it is assumed that zero net flux passes though the channel, i.e.

$$Q_1 + Q_2 = 0. \tag{2.13}$$

From this equation an expression for h_{10} can be found in terms of u_{10} and u_{20}, which will be different depending on whether the flow is separated, with the interface intersecting the bottom or the surface or both, or is fully attached, with the two layers present across the whole channel.

Results for a non-zero net flow have been described by Armi & Farmer (1986) and Farmer & Armi (1986) for the non-rotating case, and by Dalziel (1988) for a less general rotating case.

2.1. *Attached and separated cases*

Seven different positions of the interface are considered, shown in figure 2, to permit a comprehensive study of all possible flow regimes. The numbering scheme is outlined in detail in the Appendix. As a result the interval over which the flux expression (2.12) is integrated changes for each case, leading to different expressions for h_{10} for each regime.

In regime 7, a sketch of which is enlarged in figure 2, the flow is separated from both the right-hand and left-hand side of the channel and so the interface height is

defined as follows:

$$h_1 = \begin{cases} 0 & \text{for } -W/2 \leqslant y \leqslant y_b \\ (u_{20} - u_{10})y + h_{10} & \text{for } y_b < y < y_s \\ D & \text{for } y_s \leqslant y \leqslant W/2 \end{cases} \tag{2.14}$$

where y_b, y_s respectively denote the points across the channel where the interface intersects with the bottom or surface.

The vorticity equation applies in both one- and two-layer regions. Thus the velocities are continuous at both y_b and y_s (otherwise the potential vorticity would possess singularities). Hence the velocities are as follows:

$$u_1 = \begin{cases} \text{undefined} & \text{for } -W/2 \leqslant y \leqslant y_b \\ y + u_{10} & \text{for } y_b < y \leqslant W/2 \end{cases} \tag{2.15}$$

and

$$u_2 = \begin{cases} y + u_{20} & \text{for } -W/2 \leqslant y \leqslant y_s \\ \text{undefined} & \text{for } y_s < y \leqslant W/2. \end{cases} \tag{2.16}$$

Similarly the interface and velocity profiles are set up for all the other regimes.

As mentioned before, for each regime an expression for h_{10} can be derived assuming the zero-net-flux condition. We derive h_{10} for regime 7 as an example; the results for the other regimes are given in the Appendix along with a test used to determine the validity of the regime used to compute h_{10}.

For regime 7 the integrals for the fluxes are

$$Q_1 = \int_{y_b}^{y_s} u_1 h_1 \, \mathrm{d}y + D \int_{y_s}^{W(x)/2} u_1 \, \mathrm{d}y \tag{2.17}$$

and

$$Q_2 = D \int_{-W(x)/2}^{y_b} u_2 \, \mathrm{d}y + \int_{y_b}^{y_s} u_2 h_2 \, \mathrm{d}y. \tag{2.18}$$

The zero-net-flux condition $Q_1 + Q_2 = 0$ gives an expression for h_{10}:

$$h_{10} = \frac{Du_{10}(y_s - W/2) - Du_{20}(y_s + W/2) - 1/2(u_{20} - u_{10})^2 (y_b^2 - y_s^2)}{(u_{20} - u_{10})(y_b - y_s)}. \tag{2.19}$$

From equation (2.10), we find expressions involving y_s and y_b:

$$h_1(y_b) = (u_{20} - u_{10})y_b + h_{10} = 0, \tag{2.20}$$

$$h_1(y_s) = (u_{20} - u_{10})y_s + h_{10} = D, \tag{2.21}$$

and solving for y_s and y_b:

$$y_b = -\frac{h_{10}}{u_{20} - u_{10}}, \tag{2.22}$$

$$y_s = \frac{D - h_{10}}{u_{20} - u_{10}} = \frac{D}{u_{20} - u_{10}} + y_b. \tag{2.23}$$

On substituting (2.23) into (2.19), h_{10} simply reduces to

$$h_{10} = \tfrac{1}{2}(D + u_{10}W + u_{20}W), \tag{2.24}$$

The flux in the bottom layer for regime 7 becomes

$$Q_1 = \frac{(D-h_{10})^3 + h_{10}^3}{3(u_{20}-u_{10})^2} + \frac{u_{10}(u_{20}-u_{10})+h_{10}}{2(u_{20}-u_{10})}\left[(D-h_{10})^2 - h_{10}^2\right] + \frac{h_{10}u_{10}D}{u_{20}-u_{10}} + \frac{1}{2}\left[\frac{W^2}{4} - \left(\frac{D-h_{10}}{u_{20}-u_{10}}\right)^2\right] + u_{10}\left[\frac{W}{2} - \frac{D-h_{10}}{u_{20}-u_{10}}\right]. \quad (2.25)$$

Equation (2.24) can be substituted for h_{10} in equation (2.25) to find the flux purely in terms of u_{10} and u_{20} and the geometry variables, W and D.

For the fully attached flow (regime 5) the flux is given by the much simpler expression

$$Q_1 = \frac{L^3}{12}(u_{20}-u_{10}) + Lu_{10}h_{10}. \quad (2.26)$$

Similar (but clearly not identical) computations of the fluxes have been done for all other regimes. However, computations of the fluxes for the results presented in § 3 were made numerically without deriving each individual flux expression, to reduce the risk of algebraic errors. The numerical error is less than 1×10^{-5} for the flux results, i.e. the magnitude of the fluxes which will be presented in this paper are accurate up to at least five decimal places. We also consider only the regimes which have a positive slope, $h_s = (u_{20} - u_{10}) > 0$, and thus conform with our assumption of northern hemisphere rotation; these regimes are 4, 5, 7 and 8.

The flux, because it is a conserved quantity, will be taken as the first functional in terms of the two variables u_{10} and u_{20}. Generally we will use expressions for the flux in the bottom layer Q_1 given by the integral (2.12) with $i = 1$. The second functional needed comes from the conservation of the Bernoulli potential.

2.2. *Bernoulli potential*

Integrating the along-channel momentum equations with respect to x gives

$$\tfrac{1}{2}u_1^2 + (P + h_1 - D) = E_1 \quad (2.27)$$

and

$$\tfrac{1}{2}u_2^2 + P = E_2. \quad (2.28)$$

On subtracting them we find

$$E_1 - E_2 = \tfrac{1}{2}\left(u_1^2 - u_2^2\right) + h_1 - D \quad (2.29)$$

where E_1 and E_2 are the Bernoulli constants for the bottom and top layer respectively. They are independent of both x and y for zero potential vorticity, and hence must be constant over the entire flow, unless a hydraulic jump occurs.

Substituting the linear expressions for u_1, u_2, and h_1 into (2.29) results in the following expression:

$$\Delta E = E_1 - E_2 = \tfrac{1}{2}\left(u_{10}^2 - u_{20}^2\right) + h_{10} - D. \quad (2.30)$$

Ideally ΔE would be a measure of the flow conditions in the upstream basin, e.g. the interface height far away from the controlled flow at the sill. It would allow us to directly work with the dependence of the flow on upstream basin conditions. This is common practice for non-rotating flows. It remains traditional practice in rotating flows also, although there are difficulties in connecting with upstream basins (cf. § 4).

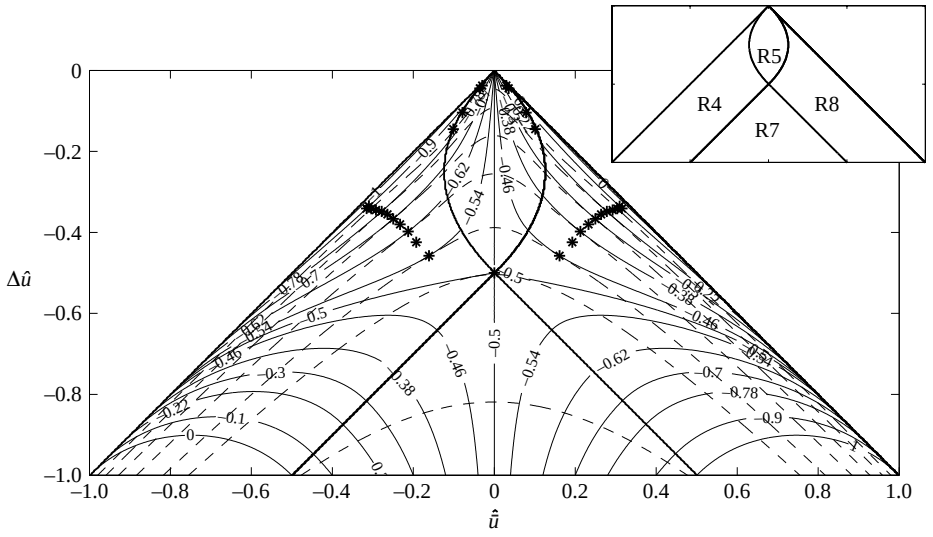

FIGURE 3. Solutions for the scaled flux $\hat{Q}_1$ (dashed lines) and Bernoulli function $\Delta\hat{E}$ (thin solid lines) for a range of $\hat{\bar{u}}$ and $\Delta\hat{u}$ in a channel cross-section with $L = 1.0$. The thick solid lines indicate points of separation and the plot inset at the top of the figure shows which regime occurs in the respective regions, where R stands for 'regime'. At some points the flux and energy lines are tangential and the pairs of $\Delta\hat{E}$ and $\hat{Q}_1$ at those points are the controlled flows; they are indicated by small asterisks. Figure 4 shows the range of selected pairs of controlled solutions, plotting $\Delta\hat{E}$ and the corresponding $\hat{Q}_1$.

3. Solutions in the pseudo-Froude-number plane

Formally the location of the primary control in a hydraulically controlled flow can be found by applying the Jacobian, as used by Pratt & Helfrich (2005), to the functions of Q_1 and ΔE, i.e.

$$\nabla Q_1 \times \nabla \Delta E = \frac{\partial Q_1}{\partial u_{10}}\frac{\partial \Delta E}{\partial u_{20}} - \frac{\partial Q_1}{\partial u_{20}}\frac{\partial \Delta E}{\partial u_{10}} = 0. \tag{3.1}$$

This means that at points where Q_1 and ΔE are tangential in the (u_{10}, u_{20})-plane, the flow is controlled.

In figure 3 the results for

$$\hat{Q}_1 = Q_1(D_0/D)^2 \tag{3.2}$$

(dashed lines) and

$$\Delta\hat{E} = \Delta E(D_0/D) \tag{3.3}$$

(thin solid lines) are contoured in the $(\hat{\bar{u}}, \Delta\hat{u})$-plane for scaled width $L = 1.0$. Here $\hat{\bar{u}} = \bar{u}(a_0/a)$ and $\Delta\hat{u} = \Delta u(a_0/a)$ (see equation (2.3)) where $\bar{u} = (1/2)(u_{10} + u_{20})$ and $\Delta u = (1/2)(u_{10} - u_{20})$. In the non-rotating theory it is conventional to use the Froude numbers for the representation of the solution space, i.e. u_{10} and u_{20}. However, when rotation is included Δu has a direct significance for the flow because it describes the slope of the interface between the two layers. The asterisks in figure 3 indicate points where a pair of contours $\Delta\hat{E}$ and $\hat{Q}_1$ are tangential and thus equation (3.1) applies. The values of $\hat{\bar{u}}$ and $\Delta\hat{u}$ at this point describe a controlled flow. The dashed lines are not labelled for clarity; however, the controlled fluxes corresponding to each of the $\Delta\hat{E}$ contours plotted are given in figure 4. The thick solid lines in figure 3 indicate transitions from fully attached to semi-separated to fully separated flows, and the small

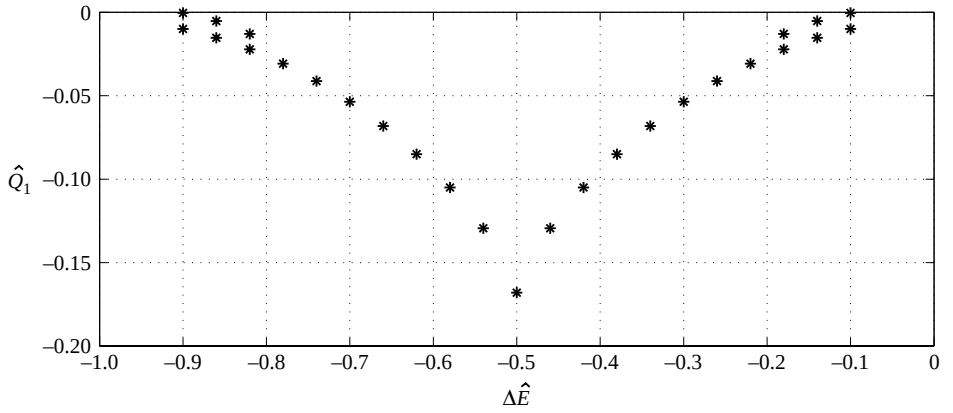

FIGURE 4. Plot of the controlled fluxes $\hat{Q}_1$ for a range of $\Delta\hat{E}$ in a channel cross-section with $L = 1.0$ corresponding to the asterisks marked in figure 3. Note that there are two controlled fluxes for $|\Delta\hat{E}| < 0.2$ and > 0.8, and the maximum flux occurs at $\Delta\hat{E} = -0.5$ where $\hat{Q}_1 = -0.167$.

inset shows which regimes apply in the different regions of the plot. In figure 3 all the controlled flows lie in regimes 4 and 8. Note that in order to be able to plot the solutions in this way we are assuming that u_{10} and u_{20} exist at every section along the channel, even though we later redefine the velocities in regimes 4 and 8 in regions where one of the layers vanishes. The new velocities in such regions were given in equations (2.15) and (2.16).

The plot resembles a rotated version of the Froude-number plane discussed by Armi (1986). However, instead of using the squared Froude numbers to plot the results, we use the pseudo-Froude numbers of the solutions at the centre of the channel, $y = 0$. The solid line in figure 3 extending from $(-1, -1)$ to $(0, 0)$ is the axis $\hat{u}_{10}$ (i.e. $\hat{u}_{20} = 0$) and the line from $(0, 0)$ to $(1, -1)$ the axis $\hat{u}_{20}$ (i.e. $\hat{u}_{10} = 0$).

The contours of the Bernoulli function in figure 3 are the same as in Armi's Froude-number plane for the non-rotating two-layer exchange, since equation (2.29) is identical in the non-rotating case and the zero-potential-vorticity rotating case. The flux contours differ; although approximately the same shape, the values in the rotating case are much lower, because rotation modifies the across-channel structure of the interface, and different non-dimensionalizations are relevant for the rotating case.

As in the non-rotating case, the controlled fluxes are equal for values of ΔE and the corresponding value $-(1 + \Delta E)$. A qualitative difference from the non-rotating case is that for a small range of ΔE there are two associated controlled fluxes, as can be seen in figure 3. The second controls, with the smaller fluxes, lie in the fully attached region (the second set of asterisks) at the tip of the plot. They arise as the flux contours become steeper in slope around $(1/2)(u_{10} + u_{20}) = 0$ to form a 'nose' in shape; as a result another Bernoulli contour will be tangential to some of the flux contours. One example in a channel of width $L = 1.0$ is the $\Delta E = -0.86$ line which is tangential to $Q_1 = -0.01533$ as well as $Q_1 = -0.00522$. The smaller of the two is not traceable away from the control section and we therefore do not consider these physically realizable solutions.

In figure 5 the flux and energy contours are shown for a channel of width $L = 0.5$. The oval regions at the tip of the plot containing the fully attached flows have increased significantly and extend beyond the boundaries of the figure. Again the

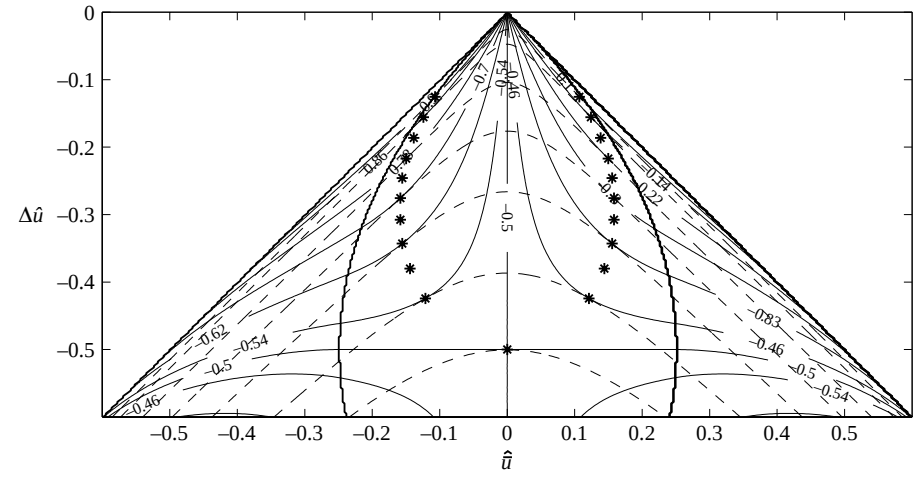

FIGURE 5. Same as figure 3, but for a cross-section with $L = 0.5$. The controlled flows lie within the fully attached region.

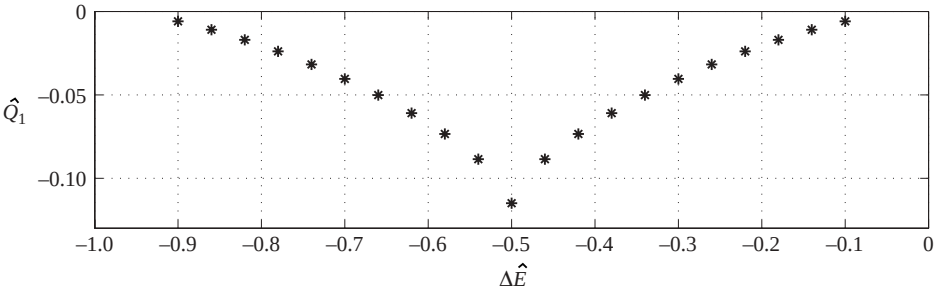

FIGURE 6. Plot of the controlled fluxes $\hat{Q}_1$ for a range of $\Delta\hat{E}$ in a channel cross-section with $L = 0.5$ corresponding to the asterisks marked in figure 5. The maximum flux occurs at $\Delta\hat{E} = -0.5$ where $\hat{Q}_1 = -0.115$.

asterisks indicate the control points and the value of the controlled flux for each energy line plotted is given in figure 6.

The maximum controlled flux for a channel of scaled width $L = 1$ is $\hat{Q}_1 = -0.167$ with $\Delta\hat{E} = -0.5$ while it is $\hat{Q}_1 = -0.300$ for $L = 1.5$, but only $\hat{Q}_1 = -0.115$ for $L = 0.5$. For both $L = 1.5$ and $L = 1$, the controlled flows are mainly semi-separated or fully separated, as opposed to fully attached for the channel of width 0.5.

Although this way of determining the controlled flows tells us the maximum possible controlled flux at $\Delta\hat{E} = -0.5$, it does not tell us whether this controlled flow is also traceable along the channel away from the primary control. We now show how to use the pseudo-Froude-number planes (figures 3 and 5) to trace the flow along the channel.

3.1. *Special traceable case*

In general the value of L will vary along the channel and, in contrast to the non-rotating problem, it is not possible to represent a complete solution on a single pseudo-Froude-number diagram. However, if the width of the channel is everywhere proportional to the square root of the depth, i.e. the topography is self-similar, then $L = \text{const.}$ and these plots can be used in the same way as those in the non-rotating case.

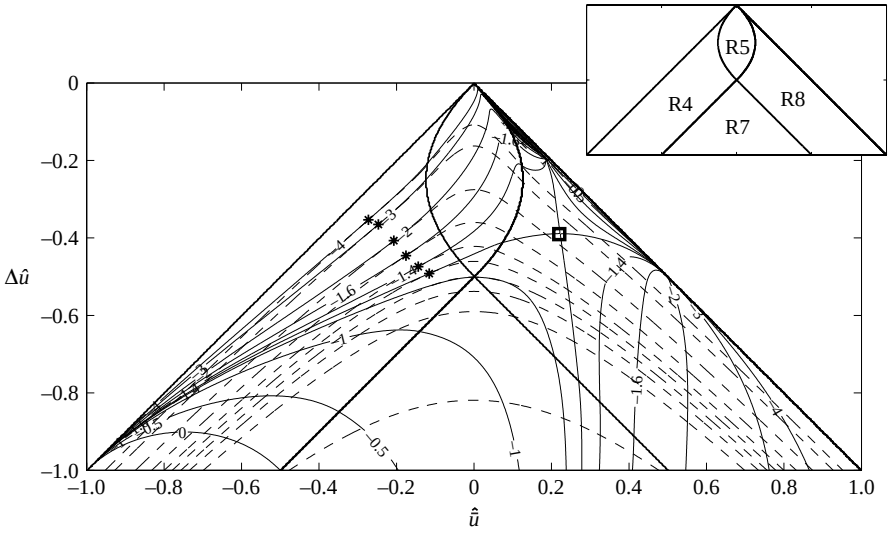

FIGURE 7. Plot showing the $\hat{Q}_1$ contours (thin dashed lines), and the solution lines, $\Delta E/\sqrt{|Q_1|}$ (thin solid lines), for a rectangular rotating channel with $L = 1.0$ everywhere. For this particular case the flow can be traced along a channel with self-similar topography using the solution lines in a single diagram, similarly to the non-rotating case. The thick solid lines mark points of transition from one regime to another as in figure 3. Again the primary controls are indicated by asterisks; the virtual control is indicated by a square. Only the solution lines are labelled and the corresponding flux values are listed in table 1.

As the depth, D, varies along the channel so do $\hat{Q}_1$ and $\Delta\hat{E}$. However, it can be shown from equations (3.2) and (3.3) that the ratio $\Delta\hat{E}/\sqrt{|\hat{Q}_1|} = \Delta E/\sqrt{|Q_1|}$ is a conserved quantity independent of D, hence the flow may be traced along isolines of this ratio.

The tracing of the flows along the solution lines was undertaken numerically, by scanning finely tabulated values of $\Delta\hat{E}/\sqrt{|\hat{Q}_1|}$ across the entire domain of $\hat{\bar{u}}$ and $\Delta\hat{u}$ to find intervals containing the desired contour value of the solution line. Linear interpolation then gives the values of $\hat{\bar{u}}$ and $\Delta\hat{u}$. At the same locations of the interval containing the solution line we pick the corresponding values of the flux, and again linearly interpolate to determine the flux along the solution line to greater accuracy. We thus arrive at a set of points describing the location, in terms of $\hat{\bar{u}}$ and $\Delta\hat{u}$, of the solution line. At the primary control $D = D_0$ and so the flux $Q_1 = \hat{Q}_{10}$ and $\Delta E = \Delta\hat{E}_0$. The depth D, and hence $\bar{u}$ and Δu, at other points along the solution line may then be determined by noting that $D/D_0 = \sqrt{Q_1/\hat{Q}_1}$.

3.2. *Channel with* $L = 1.0$

In figure 7 the contours of flux, $\hat{Q}_1$, and $\Delta E/\sqrt{|Q_1|}$ are plotted with thin dashed and solid lines respectively. The latter contours are the solution lines along which the flows can be traced as described in the previous section. As before, the thick solid lines present points of separation of the interface from the sidewalls and the asterisks mark the controls. In table 1 the values of the contoured solution lines are listed together with the corresponding value of the controlled flux and ΔE.

In a channel whose depth and width are changing as described earlier, the flow with $\Delta E = -0.5$ corresponds to the flow along contour $\Delta E/\sqrt{|Q_1|} = -1.225$ which is not

$\frac{\Delta E}{\sqrt{\lvert Q_1 \rvert}}$	ΔE	Q_1
−4	−0.7590	−0.03601
−3	−0.6983	−0.05416
−2	−0.6058	−0.09176
−1.6	−0.5542	−0.12003
−1.4	−0.5250	−0.14058
−1.3035	−0.51069	−0.15350
−1.225	−0.5002	−0.1667

TABLE 1. Table of the values of the controlled flows contoured in figure 7. Column one lists the value of the solution lines, column two the Bernoulli potential and column three the corresponding controlled flux.

traceable as can be seen in figure 7. The first traceable flow in figure 7 is that along solution line −1.3035, which is also the maximal flux for the given geometry. This solution line is the thin solid line passing through both a primary control, marked by an asterisk, and a virtual control, marked by the square. Other flows along solution lines such as −1.4 are also traceable, but they are submaximal. Farmer & Armi (1986) have similarly shown that for non-rotating flow over a sill the solutions are only traceable for ΔE somewhat larger than 0.5.

3.2.1. *Maximal flow*

The solutions for the maximal flow upstream and downstream from the primary control are given in figure 8 in terms of Δu (black) and $\bar{u}$ (grey) as a function of the depth D of the channel. Notice that $\Delta u = (-1/2)h_s$ is always less than 0, and hence h_s is positive, as we assumed earlier.

In general the flows will consist of three solution branches, described equally well by Δu or $\bar{u}$, two supercritical (marked with a double-headed arrow) and one subcritical (single-headed arrow), as shown in the figure. The direction of the arrows indicates the direction of the net flow in the bottom layer. Those that point to the left lie along the upstream solution branches of which there are two, one supercritical and one subcritical. These two meet at a virtual control marked by a vertical line. The flow then approaches the primary control at the top of the sill or at the contraction (marked by a second vertical line). Between the virtual and primary control the flow passes briefly through a region where it can only be subcritical. After the primary control the solution line turns back on itself and moves downstream as a supercritical flow (marked by a double-headed arrow pointing right).

What does figure 8 tell us about the flow along the channel? Where the downstream branch approaches $D = 7$, we find that $\bar{u} \simeq \Delta u$, $\bar{u} - \Delta u = u_{20} \simeq 0$. The top layer therefore has approximately zero velocity at the centre of the channel far downstream and on either side of the zero-velocity line significant flow will be directed in opposite directions. Similarly, $\bar{u} + \Delta u = u_{10} \simeq -5$ which leads us to conclude that the velocities in the bottom layer are everywhere negative, since $u_1 = y + u_{10}$ and y has a maximum value of $\sqrt{D}/2 = \sqrt{7}/2 = 1.32$.

Far upstream of the primary control, as D increases $\bar{u}$ approaches $-\Delta u$, meaning that $u_{10} \simeq 0$ and u_{20} will have a large positive value. This applies for both supercritial and subcritical branches of the flows. Thus the bottom layer will now have a significant region of backflow upstream and the top layer will also still have some backflow,

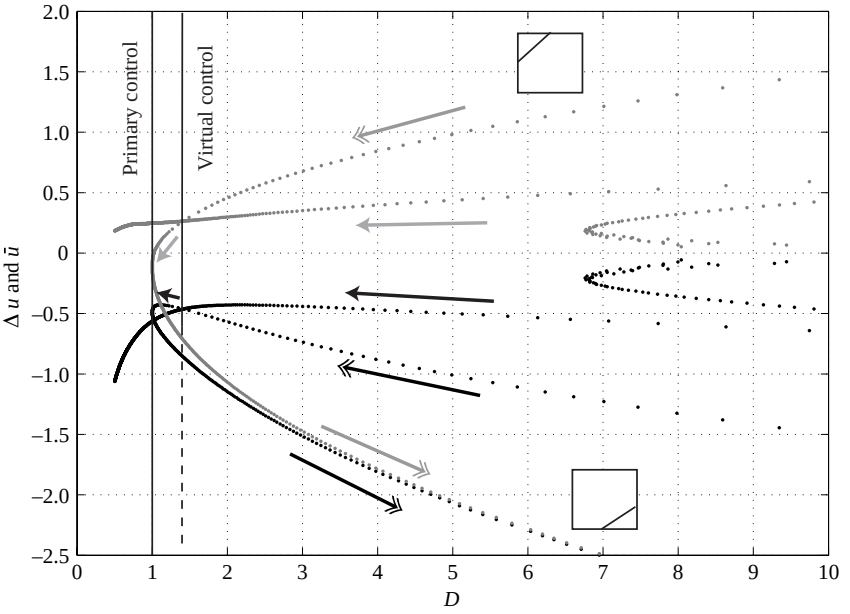

FIGURE 8. Plot of Δu in black, and $\bar{u}$ in grey, against the depth of the channel, for a flow with $L = 1$ and $\Delta E/\sqrt{|Q_1|} = -1.3035$. The primary control is at $D = 1$ where for both Δu and $\bar{u}$ only two solutions (roots) exist. The secondary control occurs at $D \sim 1.4$, where again two out of the three roots coincide. The two dotted lines marked by double-headed arrows pointing right are the supercritical downstream solutions of the flow, where the flow is separated from the right-hand wall (see inset). Upstream the flow is briefly subcritical (single-headed arrow) until it encounters the second control; from here the flow can follow either a supercritical branch (single-headed arrows pointing left) or a subcritical branch (double-headed arrows pointing left). In both the supercritical and the subcritical case the interface will outcrop at the surface. The arrows indicate the net flow direction of the bottom layer.

however not as significant as downstream. (The treatment of backflows is postponed to § 4.)

All branches in figure 8 can be identified with sections of the contours in figure 7. The part of the -1.3035 contour that extends from $(-1, -1)$ to the point where it is tangential to the flux contour, $Q_1 = -0.1545$, corresponds to the flow downstream of the sill. Hence the flow downstream including the control is semi-separated in regime 4.

The top of the sill is where the flux and solution contours are tangential in figure 7 and this point is marked as 'primary control' in figure 8.

As we move past the primary control on figure 7 the -1.3035 contour passes through a brief region of fully attached flow, before it reaches a point where it intersects another solution line of the same value. The line that leads straight on and approaches the $u_{10} = 0$ axis corresponds to the supercritical dotted lines (double-headed arrow) of the upstream solution. The contour extending upwards towards the tip of the diagram corresponds to the subcritical upstream lines (single-headed arrow) of the upstream solution. From figure 7 we see that both upstream solution branches, super-and subcritical, are semi-separated in regime 8.

Armi (1986) postulates that following the contour toward the $u_{10} = 0$ axis leads to the maximal flux solution which is also fully controlled, with a supercritical region upstream, while following the contour that extends upwards also results in a flow with

the maximum flux, but having submaximal flow features, i.e. the flow is subcritical everywhere upstream. This is confirmed in our rotating case.

The third branch leading away from this intersection on figure 7 extends down towards (0.25, −1.5). The solutions on this contour correspond to the dotted lines in figure 8 that extend from the virtual control into the region $D < 1$. These solutions do not represent any physically realizable regimes of the flow and can be ignored. For sections with $D > 6.7$ another set of solutions appear, from a contour located at the tip of figure 7, which can only be distinguished if we zoom in closer onto this region. Figure 8 shows, however, that these solutions have no connection to the flow we are tracing and so we can disregard them in our discussion.

To conclude the description of the maximal flow along the channel it is worthwhile to relate this graphical representation of the solutions to the solutions one would obtain by solving the functionals.

Notice that for each D in figure 8 these are several values for both $\bar{u}$ and Δu; for the most part (between $D = 1$ and ~ 6.7) there are three values for both of these parameters, with two important exceptions: on the lines $D = 1$ and $D \sim 1.43$ there are only two. These are the primary and virtual controls respectively, as indicated in the figure. Essentially, each dot in the figure corresponds to a root of the functional; if two coincide, we encounter a control point! After each control the flow has the potential to follow a super- or a subcritical path. At the primary control the flow splits into the downstream flow, which is always supercritical, and the upstream flow, which briefly moves along a subcritical path. It then encounters the secondary or virtual control and again can follow either a supercritical path, which links continuously to the subcritical regions, or the subcritical path. Both of these are valid paths of the flow and both can carry the same, maximal, amount of flow.

When the value of the solution line is increased by a small amount the upstream solutions branches no longer meet and so no virtual control is possible. We now describe an example of such a purely submaximal flow.

3.2.2. *A submaximal case*

As an example of a submaximal flow we choose to trace $\Delta E/\sqrt{|Q_1|} = -1.400$, and the solutions at each cross-section of this flow are shown in figure 9. In contrast to the maximal case, in the submaximal case the subcritical branch of the upstream solution never intersects with the supercritical solution to allow a transition from subcritical to supercritical flow.

Again the dotted lines in the figure can be identified with certain sections of the solution line −1.400 of figure 7. The contour for the downstream flow lies to the left of the tangential point marked by the asterisk on the solution line. Beyond this primary control the solution line moves up into the fully attached region and then into regime 8 but never intersects another contour of the same value, which again indicates that no transition to a supercritical flow is possible.

The flow features are in general similar to those encountered in the maximal flow case with $\bar{u} \simeq \Delta u$ far downstream, and hence $\bar{u} - \Delta u = u_{20} \simeq 0$, leading to the same conclusions regarding the velocities and direction of the flow.

The interface height between the two layers and the velocity fields are plotted in figure 10. Figures 10(*a*) and 10(*d*) illustrate that the flow passes through three different regimes along the channel, moving from regime 8 far upstream (at the top of the figures) into 5, and finally regime 4 downstream (at the bottom of the figures).

In figure 10(*b*) the formation of the separated boundary current in the bottom layer can be seen, also illustrating that the backflow does not extend across the sill. This

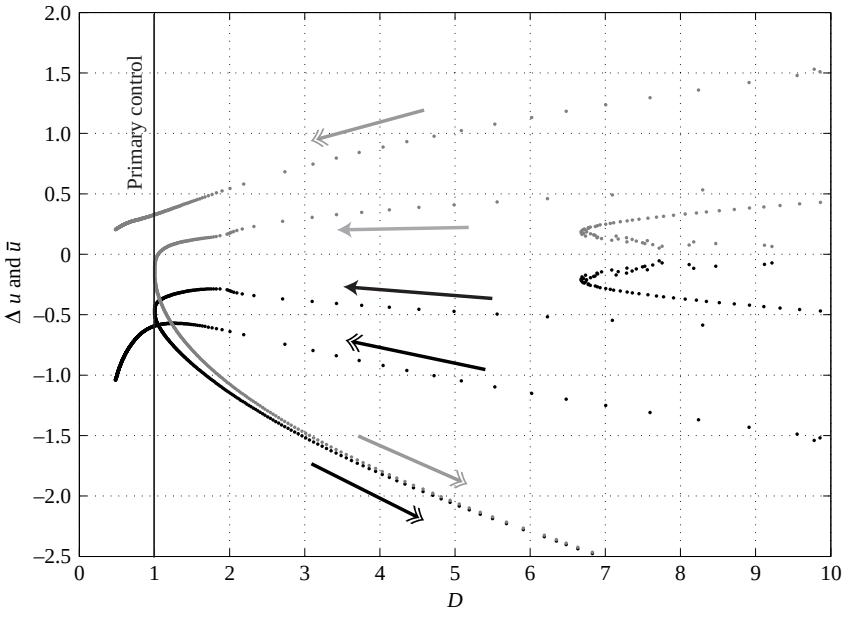

FIGURE 9. Along-channel results of a flow with $L = 1$ and $\Delta E/\sqrt{|Q_1|} = -1.400$. The lines and arrows are the same as in figure 8, and the controlled flow is $Q_1 = -0.141$ in this case. This flow is submaximal since supercritical and subcritical branches of the upstream do not intersect to allow for a virtual control.

is always the case for the bottom layer at the primary control if the flow is regime 4 or 5. In figure 10(*c*) the boundary current in the top layer is featured upstream of the sill and in contrast to the bottom layer there is a region of backflow on the right-hand side all along the channel. It can be said in general that if the flow over a sill is semi-separated (regime 4) at the control then the top layer will contain a considerable region of backflow along the entire length of the channel.

3.2.3. *Untraceable cases*

In addition to the traceable cases there are two types of flows which are not traceable. One is 'almost' traceable, in the sense that both upstream and downstream branches can be discerned on a diagram like figure 9 but there is a jump in one branch which renders the flow discontinuous and thus non-traceable. These types of flows occur for certain $\Delta E/\sqrt{|Q_1|} < -1.3035$.

In the second case the upstream branch of the flow is missing completely, indicating that there is only one root for most of the cross-sections and the downstream flow cannot be connected to any kind of flow upstream. More details on these untraceable cases can be found in Riemenschneider (2004).

3.3. *Channel with* $L = 0.5$

The solution lines for a channel of width $L = 0.5$ are plotted in figure 11; here the maximal flow has $\Delta E/\sqrt{|Q_1|} = -1.55054$ as listed in table 2, which corresponds to $\Delta E = -0.5066$. Notice that this is less than the maximal ΔE for a channel with $L = 1.0$ which was found to be -0.51069. So as the (non-dimensional) channel width decreases, i.e. the rotation rate decreases, the closer the flux approaches – but remains less than – the flux at $\Delta E = -0.5$, the maximum achievable.

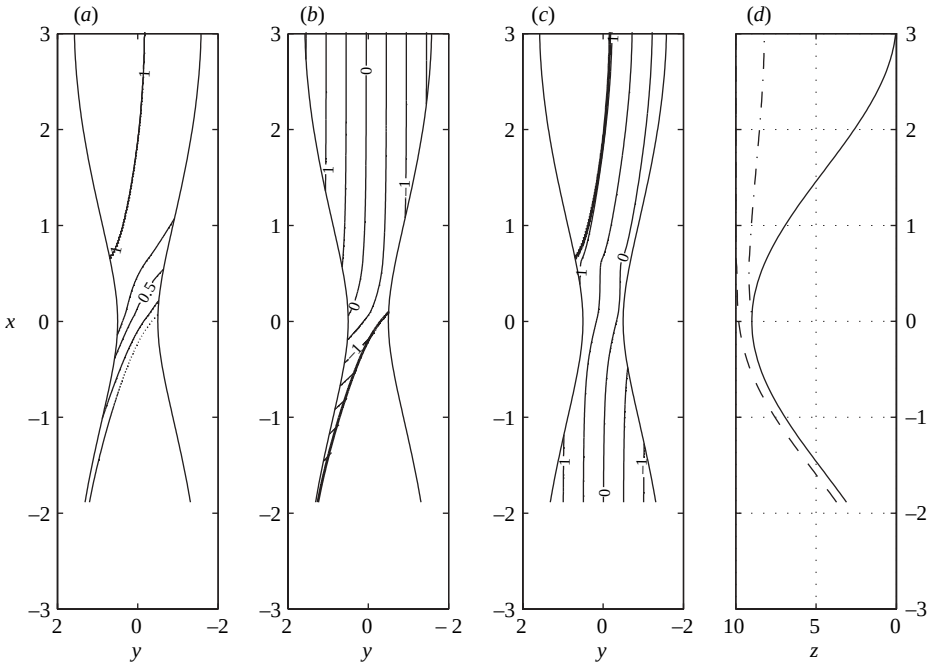

FIGURE 10. The features of a submaximal flow through a channel with $L = 1$ and $\Delta E/\sqrt{|Q_1|} = -1.40$. A contour plot of the bottom layer thickness is shown in (*a*) as a fraction of the channel depth, hence to the left of contour 1 the top layer vanishes. The contour interval (c.i.) is 0.25. (*b*) The velocity field in the bottom layer which separates from the right-hand wall just before the sill and remains separated as a boundary current indicated by the thicker solid line (c.i. 0.5). (*c*) The velocity field in the top layer which vanishes upstream to the left of the thicker solid contour (as in *a*), c.i. 0.5. (*d*) Shown as a dashed line is the intersection of the interface with the left-hand wall and as a dashed-dotted line the intersection with the right-hand wall above the topography (solid line).

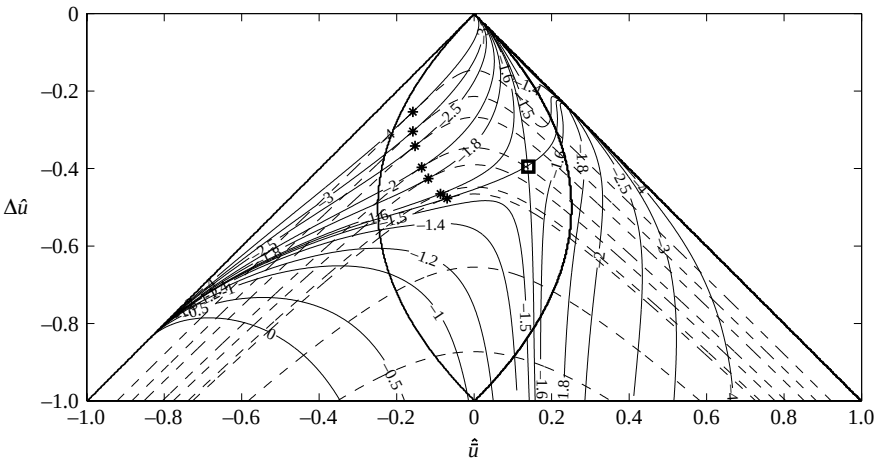

FIGURE 11. Pseudo-Froude-number diagram for a channel with $L = 0.5$ everywhere. The contours have the same meaning as in figure 7 and again the asterisks mark the solutions at the primary control and the square the virtual control. Only the solution lines are labelled and the corresponding flux values are listed in table 2.

$\dfrac{\Delta E}{\sqrt{\lvert Q_1\rvert}}$	ΔE	Q_1
−4	−0.7316	−0.03346
−3	−0.6643	−0.04901
−2.5	−0.6189	−0.06130
−2	−0.5633	−0.07933
−1.8	−0.5381	−0.08939
−1.6	−0.51245	−0.10261
−1.55054	−0.5066	−0.10674

TABLE 2. Table of the values of the controlled flows contoured in figure 11. The columns are as in table 1.

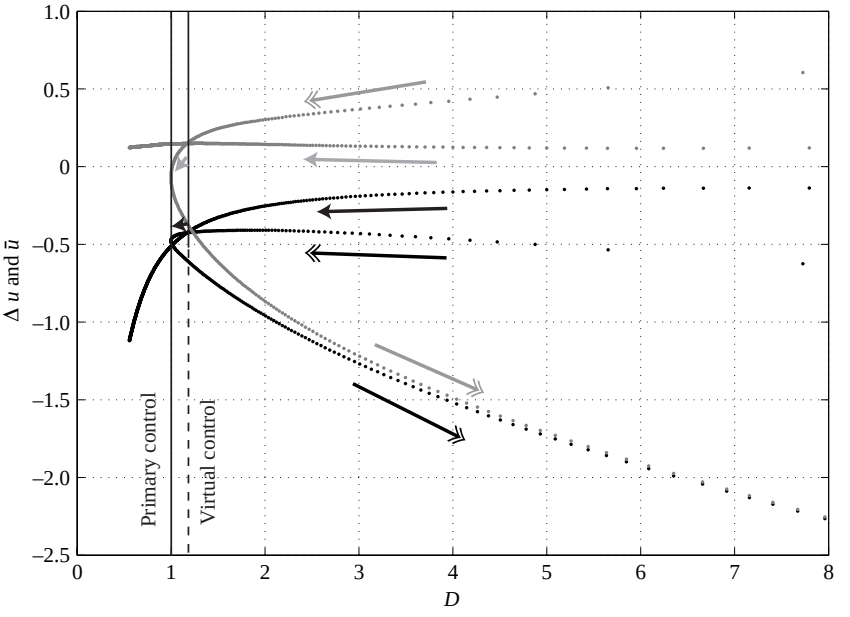

FIGURE 12. Plot of Δu (black) and $\bar{u}$ (grey) against the depth of the channel, for the maximal flow in a channel with $L = 0.5$, where $\Delta E/\sqrt{|Q_1|} = -1.55054$. The primary control is as usual at $D = 1$. The secondary control occurs at $D \sim 1.2$, where the supercritical and subcritical upstream branches intersect.

3.3.1. *Maximal case*

In figure 12 the maximal solution along the solution line −1.55054 is plotted as a function of depth. As in the previous example for a width $L = 1.0$, we can easily identify the virtual control, which occurs upstream, very close to the top of the sill where the super- and subcritical branches meet. Again this point corresponds to the point in figure 11 where the solution line −1.55054 forms an intersection (saddle point). For all other purposes the maximal solutions for both the wide and narrower channel are similar in terms of the distribution of the velocities along the channel, the major difference being only that in the narrower channel the flow is attached at the primary and secondary control, and for a significant region before and after these controls, while it is separated at both controls in the wider channel.

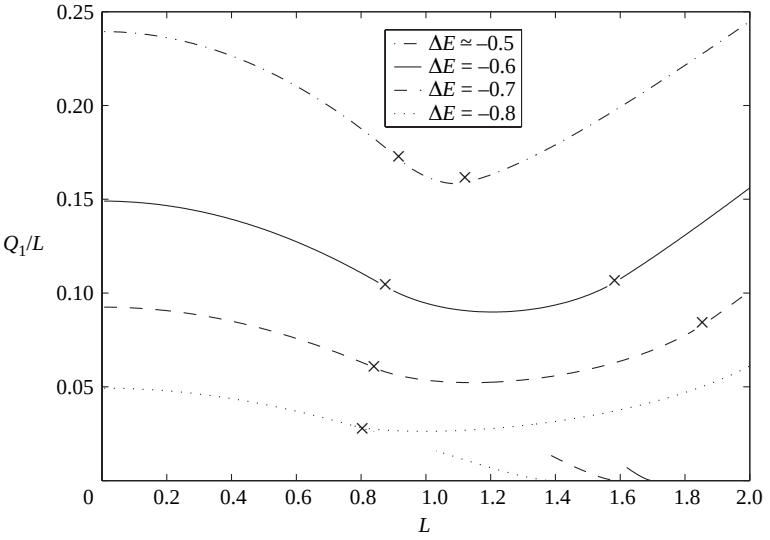

FIGURE 13. Controlled fluxes for four constant values of $\Delta E = [-0.5, -0.6, -0.7$ and $-0.8]$ over a range of L. At $L \sim 0.8$–0.9 the flows separate from the right-hand wall, indicated by the first 'x' on the curves, and subsequently the fluxes start increasing rapidly. At the second 'x' the flow becomes completely separated. A second control occurs for some ΔE at $L > 1.0$. These have very small fluxes and prevent flow with a flux less than ~ 0.015 being traceable beyond this second control.

3.4. *Comprehensive flux results*

For any application of this theory to actual overflows the quantity of interest is the flux or transport of water mass through a given channel or over a sill. In figure 13 fluxes as a fraction of channel width L are plotted for a range of Bernoulli potentials ΔE and widths L. Although it is relatively easy to read off any controlled flux from this plot it is not possible to determine whether the flow will be traceable along the channel, or indeed where the maximal flow lies.

In the previous section we showed that the maximum flow possible through a control section occurs for $\Delta E = -0.5$; however this solution was shown to be non-traceable in the examples discussed. The line of maximal flows will lie somewhat below the dashed-dotted line for $\Delta E \sim -0.5$ in figure 13, and the exact values will depend on the geometry of the channel. All other flows below the maximal curve are submaximal and the majority will be traceable.

The figure shows that as $L \to 0$ the non-rotating limit of $Q/L = 0.25$ is approximately approached by the solutions for $\Delta E \sim -0.5$. For numerical reasons we are unable to compute the flux for $\Delta E = -0.5$ exactly, but in fact show the flux for $\Delta E = -0.503$ in figure 13. Because of this and due to added numerical errors, the flux does not exactly approach 0.25 in the non-rotating limit. However, we can show the limit analytically from equation (2.26). Dividing the expression by L and then letting L on the right-hand side go to 0 we find $Q_1/L = u_{10}h_{10}$. As $L \to 0$, u_{10} and $h_{10} \to 0.5$ and hence $Q_1/L \to 0.25$.

The fact that the flux increases rapidly as the width of the channel exceeds $L \sim 1$ makes the theory difficult to apply for wide channels. Dalziel (1988) excludes backflow and finds that solutions to this kind of flow show a flux that levels off and stays constant beyond $L = 1.0$.

Another result which we believe is unique to the solutions including backflow is the occurrence of a second controlled flow for some ΔE at small ranges of L. These will render the flow untraceable beyond the point where this extra controlled flow is encountered. This applies to all controlled flows with $|Q_1| < 0.015$.

4. Discussion

A new way of showing the solutions for two-layer rotating exchange flows in a pseudo-Froude-number plane has been presented for semi-geostrophic, zero-potential-vorticity flows. All possible separations of the flow from the sidewalls of a rectangular channel were considered, and subcritical, critical and supercritical solutions were shown.

The maximum flux for any given topographic cross-section occurs for $\Delta E = -0.5$ which agrees with the findings by Armi & Farmer (1986) for the non-rotating case. However the flow at $\Delta E = -0.5$ was shown not to be traceable for flow over a sill. Traceable values of ΔE depend on the channel geometry and the strength of rotation.

The solutions in the pseudo-Froude-number plane depend upon the ratio, L, of the channel width to the Rossby radius. Thus, in contrast to the non-rotating case, it is not in general possible to trace solutions along the length of the channel in one diagram. However, when the topography is self-similar in such a way that the channel width is proportional to the square root of the depth, then L is constant and solutions may be traced along the entire channel using a single diagram. These cases provide significant insight into rotating exchange flows over sills.

We considered two examples of channels with L constant, first a relatively wide channel with $L = 1$, and then a narrower channel with $L = 0.5$. In the latter case the flow was attached to both walls at the sill for all realizable solutions, including the maximal exchange. However, the lower layer did, in all cases, separate from the right-hand wall somewhere downstream of the sill. For submaximal flows in the wider channel ($L = 1$) the interface was attached to both walls for a small region upstream of the sill, but separated from the left-hand wall eventually. Both maximal and submaximal solutions for $L = 1$ separate from the right-hand wall before reaching the primary control.

Our theory possesses the same shortcoming as most rotating hydraulics studies. Virtually all distributions of potential vorticity are inconsistent with a sluggish upstream basin (cf. Killworth 1992*a* for the only extant one-layer solution satisfying this condition), although in practice all controls occur near the sill where our theory holds. The justification often given for studies of zero potential vorticity dates from Whitehead *et al.* (1974) who assumed that an infinitely deep upstream basin gave rise to zero-potential-vorticity flow. However, their (and many other later) solutions require a non-zero relative vorticity everywhere and so cannot match to a sluggish upstream situation. How to achieve such a match, which must involve a transition from a two-layer flow in the channel to a single-layer flow above and below an infinitely deep stagnant layer in the upstream and downstream basins respectively, is beyond the scope of this paper, and remains a thorny issue.

Timmermans & Pratt (2005) have attempted to connect controlled two-layer solutions at the sill in a constant-width channel to single-layer conditions in the upstream basin, where the lower layer is deep and stagnant and only the top layer is dynamically important. In doing so they assume that the secondary control is located at the exit of the channel; however, they do not attempt to find a continous link between the primary control at the sill and the exit control. The maximal flux derived assuming

an exit control is marginally smaller than the transport derived for a maximal flow with a virtual control over the sloping bottom of the channel. (For this study we were forced to assume $\Delta E = -h_{20}$ in the upstream basin far from the channel).

Our theory, in common with many others, also possesses ambiguities in how regions of backflow should be handled, because the origin of the water in such regions is unclear. In the case of the top layer it may either have come from the downstream basin and then reversed; or it may be trapped in a region of re-circulation; or it may have come from the upstream basin. In the last case it is not clear how information is propagated in the downstream direction, if the flow in part of the region is directed downstream.

In previous two-layer studies the problem of backflow has been dealt with in two ways. Dalziel (1988) removed it by assuming that in the region where the velocities change sign and flow is directed in the opposite direction to the mean flow within a given layer the fluid is stagnant. This method assumes that the backflow occurs only in parts of the channel where just one layer is present. Whitehead *et al.* (1974) on the other hand assumed that all regions containing only one layer are stagnant and the main flow is concentrated in a small region of the channel cross-section containing two layers. This yielded a maximum flow of $Q = g' D_0^2/6f$. The problem with this assumption is that it necessarily leads to pronounced and most likely unrealistic shear layers where the flow meets the stagnant regions.

For single-layer flow with arbitrary potential vorticity, Killworth (1994) eliminated backflow by adjusting the interface above the backflow region to be horizontal, making the flow in this region stagnant. This is not possible in the two-layer case since both layers are dynamically involved in the flow.

In field observations backflows are rarely seen in the deep overflows, which is consistent with the theory. Backflow in the surface layers may well occur in the ocean but these are probably due to other forcing mechanisms, such as wind stresses.

Laboratory experiments by Dalziel (1988) for two layers and Whitehead & Salzig (2001) and Borenäs & Whitehead (1998) for one and a half layers have shown that there are regions upstream of the sill where the bottom layer seems stagnant rather than re-circulating, but these regions do not come in contact with the sill, and this again agrees with theoretical findings. Dalziel (1988) does not describe the circulation in the top layer: like all other laboratory studies we reviewed the main focus is on the circulation in the bottom layer.

Because it is still unclear how to treat the problem of backflow we opted to include it unchanged to give an idea of where and how it influences the controls. The theory could be adapted to exclude velocities directed against the mean flow in each layer and a comparison will no doubt be valuable. Our results show that for $L < 1$ backflow in the bottom layer does not occur at the sill. For large values of L backflow does occur and in these cases solutions appear to have unrealistically large exchange fluxes.

Despite the limitations of the theory, the presentation of the solutions in a pseudo-Froude-number plane, analogous to the Froude-number plane developed by Armi (1986), adds new insight into the established theory of two-layer rotating hydraulics.

The authors would like to thank Larry Armi, Jeff Blundell, Andy Hogg, Larry Pratt and Mary-Louise Timmermans for discussions about this work and suggestions for improvements on several drafts of the thesis and paper. The comments of two anonymous reviewer have also helped to improve the structure and content of the paper. This work was carried out as part of a PhD Thesis funded by an Alumni Fund of the University of Southampton as well as a maintenance grant from the James

Rennell Division at the Southampton Oceanography Centre (NERC). It also forms part of the JRD's Core Strategic Program LSLTOC. The manuscript has Woods Hole Oceanographic Institution Contribution Number 11274.

Appendix. Determining the separated regimes

When solving the no-net-flux condition in the two-variable case, expressions for h_{10} can be derived in terms of u_{10} and u_{20}, or alternatively $\Delta u = (1/2)(u_{10} - u_{20})$ and $\bar{u} = (1/2)(u_{10} + u_{20})$. The expressions for h_{10} will differ depending on the regime the flow is in and those for regimes 2–8 are listed below. Regimes 1 and 9 are not included in our analysis, since in both only one layer is present, implying that the other layer has completely vanished. Mass conservation and the fact that we do not allow for any mixing between the layers, means that these two cases can never occur. The significance of the numbers in brackets is explained in § A.1.

Regime (2,1) – 2

$$h_{10} = -W\Delta u + \sqrt{-2WD(\bar{u} - \Delta u)}. \tag{A 1}$$

Regime (3,1) – 3

$$h_{10} = \tfrac{1}{2}D - W\bar{u}. \tag{A 2}$$

Regime (1,2) – 4

$$h_{10} = W\Delta u + \sqrt{2WD(\bar{u} - \Delta u)}. \tag{A 3}$$

Regime (2,2) – 5

$$h_{10} = -\frac{D(\bar{u} - \Delta u)}{2\Delta u}. \tag{A 4}$$

Regime (3,2) – 6

$$h_{10} = D + W\Delta u - \sqrt{2WD(\bar{u} + \Delta u)}. \tag{A 5}$$

Regime (1,3) – 7

$$h_{10} = \tfrac{1}{2}D + W\bar{u}. \tag{A 6}$$

Regime (2,3) – 8

$$h_{10} = D - W\Delta u - \sqrt{-2WD(\bar{u} + \Delta u)}. \tag{A 7}$$

A.1. *Regime numbering scheme*

The numbering of the regimes may seem arbitrary, but is designed to give an easy way to test the regimes numerically. The channel cross-section is divided into three regions as illustrated in figure 14. The first one is the region above the surface of the water, labelled 3, region 2 contains the flow and the region below the channel is labelled 1. Depending on the point of intersection of the interface with the sidewalls (and/or the extended lines of the sidewalls above and below the channel) the regime is labelled using the numbers of the regions of intersection. In the example in figure 14 the interface intersects the right-hand side of the channel and the surface, which if extended leads to an intersection with the left-hand wall above the surface, hence this regime is labelled (2,3). In order to simplify the regime determination in the numerical code, each regime was then assigned a single number using the following expression:

$$R = I_R + 3(I_L - 1). \tag{A 8}$$

Here R, denotes the case or regime, I_L the index of intersection along the left-hand wall and I_R the index of intersection along the right-hand wall. So the example in our figure has $I_R = 2$ and $I_L = 3$ and hence $R = 8$.

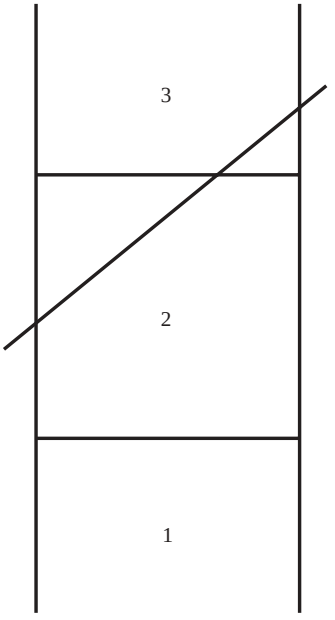

FIGURE 14. Illustration of the numbering scheme. The region above the channel is labelled 3, that below the channel 1, and the channel itself 2. According to where the interface intersects the sidewalls (and/or extended sidewalls) the flow is assigned a regime number.

A.2. *Validity of the regimes*

A brief outline of the algorithm used to determine the physically realizable solutions for the across channel profile of the flow is given here. As in § 2 the aim is to find the flux across the sill for a range of physical values of u_{10} and u_{20} (or alternatively h_s). At the outset however, we do not know which h_{10} to use as we cannot be sure what regime a particular combination of channel geometry and values of u_{10} and u_{20} will result in. The following procedure is followed to determine the relevant regime:

(*a*) For a particular geometry and range of u_{10} and u_{20}, the h_{10} are computed using the zero-net-flux assumption for all seven cases we consider.

(*b*) Together with the parameters chosen at the outset, h_{10} will describe all the physical characteristics of the flow. We therefore determine the points of intersection of the interface, given by $h_1 = (u_{20} - u_{10})y + h_{10}$, with the sidewalls of the channel.

(*c*) If these points agree with the assumptions made about the intersection points when finding h_{10} in the first place (see formulae above) then the solution is valid. If the intersection points do not agree with the initial assumptions the case is dismissed.

For some cases h_{10} is the result of a quadratic equation which will have two roots. On analysis of the roots as described above it was found that one of these roots never led to any valid cases and was therefore excluded as a possible solution for h_{10}.

REFERENCES

ARMI, L. 1986 The hydraulics of two flowing layers with different densities. *J. Fluid Mech.* **163**, 27–58.

ARMI, L. & FARMER, D. M. 1986 Maximal two-layer exchange through a contraction with barotropic net flow. *J. Fluid Mech.* **164**, 27–51.

Borenäs, K. M. & Whitehead, J. A. 1998 Upstream separation in a rotating channel flow. *J. Geophys. Res.* **103**, 7567–7578.

Dalziel, S. B. 1988 Two-layer hydraulics: maximal exchange flows. PhD thesis, Department of Applied Mathematics and Theoretical Physics, University of Cambridge.

Dalziel, S. B. 1990 Rotating two-layer sill flows. In *The Physical Oceanography of Sea Straits* (ed. L. J. Pratt), pp. 343–371. Kluwer.

Dalziel, S. B. 1991 Two-layer hydraulics: a functional approach. *J. Fluid Mech.* **223**, 135–163.

Dalziel, S. B. 1992 Maximal exchange in channels with nonrectangular cross section. *J. Phys Oceanogr.* **22**, 1188–1206.

Farmer, D. M. & Armi, L. 1986 Maximal two-layer exchange over a sill and through the combination of a sill and contraction with barotropic flow. *J. Fluid Mech.* **164**, 53–76.

Gill, A. E. 1977 The hydraulics of rotating-channel flow. *J. Fluid Mech.* **80**, 641–671.

Killworth, P. 1992*a* Flow properties in rotating, stratified hydraulics. *J. Phys. Oceanogr.* **22**, 997–1017.

Killworth, P. 1992*b* On hydraulic control in a stratified fluid. *J. Fluid Mech.* **237**, 605–626.

Killworth, P. 1994 On reduced-gravity flow through sills. *Geophys. Astrophys. Fluid Dyn.* **75**, 91–106.

Pratt, L. J. & Helfrich, K. 2005 Generalized conditions for hydraulic criticality of oceanic overflows. *J. Phys. Oceanogr.* **35**, 1782–1800.

Riemenschneider, U. 2004 Theory of two-layer rotating exchange flows – An analytical and numerical modelling study. PhD thesis, School of Ocean and Earth Science, University of Southampton.

Smeed, D. 2000 Hydraulic control of three-layer exchange flows: Application to the Bab al Mandab. *J. Phys. Oceanogr.* **30**, 2574–2588.

Timmermans, M.-L. & Pratt, L. J. 2005 Two-layer rotating exchange flow between two deep basins: Theory and application to the Strait of Gibraltar. *J. Phys. Oceanogr.* **35**, 1568–1592.

Whitehead, J. A., Leetmaa, A. & Knox, R. A. 1974 Rotating hydraulics of strait and sill flows. *Geophys. Fluid Dyn.* **6**, 101–125.

Whitehead, J. A. & Salzig, J. 2001 Rotating channel flow: Control and upstream currents. *Geophys. Astrophys. Fluid Dyn.* **95**, 185–226.

Wood, I. R. 1970 A lock exchange flow. *J. Fluid Mech.* **42**, 671–687.